



**HAL**  
open science

## Photovoltaic failure diagnosis using imaging techniques and electrical characterization

Daha Hassan Daher, Alexandre Mathieu, Asma Abdallah, Dek Mouhoumed,  
Pierre-Olivier Logerais, Leon Gaillard, Christophe Ménézo

► **To cite this version:**

Daha Hassan Daher, Alexandre Mathieu, Asma Abdallah, Dek Mouhoumed, Pierre-Olivier Logerais, et al.. Photovoltaic failure diagnosis using imaging techniques and electrical characterization. EPJ Photovoltaics, 2024, 15, pp.25. 10.1051/epjpv/2024022 . hal-04743777

**HAL Id: hal-04743777**

**<https://hal.science/hal-04743777v1>**

Submitted on 18 Oct 2024

**HAL** is a multi-disciplinary open access archive for the deposit and dissemination of scientific research documents, whether they are published or not. The documents may come from teaching and research institutions in France or abroad, or from public or private research centers.

L'archive ouverte pluridisciplinaire **HAL**, est destinée au dépôt et à la diffusion de documents scientifiques de niveau recherche, publiés ou non, émanant des établissements d'enseignement et de recherche français ou étrangers, des laboratoires publics ou privés.



Distributed under a Creative Commons Attribution 4.0 International License

# Photovoltaic failure diagnosis using imaging techniques and electrical characterization

Daha Hassan Daher<sup>1,\*</sup>, Alexandre Mathieu<sup>2,3,4</sup>, Asma Abdallah<sup>1</sup>, Dek Mouhoumed<sup>1</sup>, Pierre-Olivier Logerais<sup>5</sup>, Leon Gaillard<sup>2</sup>, and Christophe Ménézo<sup>3</sup>

<sup>1</sup> Centre d'Études et de Recherche de Djibouti, Laboratoire des Energies Nouvelles et Renouvelables, PO box: 486, Djibouti, Djibouti

<sup>2</sup> Heliocity SAS, 31 rue Gustave Eiffel, 38000 Grenoble, France

<sup>3</sup> LOCIE UMR 5271, Université Savoie Mont Blanc, CNRS, Solar Academy Graduate School, INES, 73376 Le Bourget-du-Lac, France

<sup>4</sup> CSTB, 24 Rue Joseph Fourier, 38400 Saint-Martin-d'Hères, France

<sup>5</sup> Univ Paris Est Créteil, CERTES, IUT de Sénart-Fontainebleau, 36 rue Georges Charpak, F-77567 Lieusaint, France

Received: 18 March 2024 / Accepted: 19 June 2024

**Abstract.** Inspections of 48 photovoltaic (PV) modules within a 302.4 kWp solar array were undertaken to expose the presence of defects after 12 years of operation under the harsh environmental conditions of Djibouti. To this end, a multiple-technique testing protocol was conducted including visual inspection (VI), infrared thermography (IR), current-voltage curve characterization (I-V), ultraviolet fluorescence (UVFL) and electroluminescence imaging (EL). The main visible degradation features observed were discoloration, bubbling and snail trails with occurrences of 100%, 93.7% and 2.1% respectively. According to the IR imaging results, hotspots were observed on cells affected by snail trails. IR was combined with convolutional neural network (CNN) techniques to automatically detect the different classes of failures that PV modules may experience. EL imaging reveals that the cracks of the cells underlie the observed snail trails during visual inspection and UVFL imaging. In addition, a decrease in STC power was observed after 12 yr of operation with a median reaching 5.5% corresponding to an average degradation rate of 0.46%/years. Conclusively, fault diagnosis with combined approaches of imaging and electrical techniques is crucial to prevent defects and minimize the investment losses; this will ensure uninterrupted power generation, extended service life and high safety of photovoltaic modules.

**Keywords:** Photovoltaic fault diagnosis / infrared imaging / ultraviolet fluorescence / electroluminescence / current-voltage (I-V) curves / convolutional neural network

## 1 Introduction

Access to affordable and reliable energy supplies is vital for socio-economic advancement and is also a driving factor in the ongoing transition from fossil to renewable sources. Photovoltaic (PV) energy has gained significant prominence in the renewable energy market thanks to increasingly competitive prices, abundance of the solar resource and flexibility of technology in different integration contexts. Solar energy is now utilized across industries, communities and for individual needs. Worldwide photovoltaic energy use has grown by more than 20% per yr [1], exceeding the 1 TW milestone in the global cumulative installed capacity in 2022.

Africa has long faced challenges with the sustainability of its electricity supply. Benefitting from a high solar

potential, Africa is emerging as a promising market for PV installations, with a total installed solar PV capacity of 6,235 megawatts (MW) [2], incentivized by the advantages outlined above and as an effective solution for rural electrification. A significant risk to further utilization of PV in the region is the current lack of detailed understanding regarding the long-term degradation of PV components subjected to these climate zones found in Africa.

Given the importance of the reliability and durability of PV modules, components and systems, the long-term successful utilization of the technology has been extensively studied in recent years [3–9]. The quality assurance of photovoltaic (PV) power plants should begin during the development, engineering and procurement phases, and continue through the commissioning and on to the operational lifetime of the facility. Indeed, a detailed methodology would be able to anticipate faults and help avoiding the emergence of major defects [10].

\* e-mail: [daha.enea@gmail.com](mailto:daha.enea@gmail.com)

Having an effective operation and maintenance plan is crucial for PV power plants to ensure the proper operation of PV modules, components and systems, which ultimately leads to extended operation of the plants. Naturally, minimizing degradations and mitigating failures reduce the Levelized Cost of Energy (LCOE) by increasing the operational lifetime of PV systems [11,12] and making power plants financially more viable in the long run.

However, PV systems often experience failures during their service life and those with their associated maintenance are rarely taken into account in the early phases of PV projects as mentioned by Catelani et al. [13]. PV systems degrade naturally over time due to the exposure of subcomponents to macro and micro-climatic stressors such as solar irradiation, ambient temperature, temperature cycles, humidity, soiling, pollution, heterogeneous conditions across the PV array, soiling, humidity, salt mist/gas, wind/snow, hail and so on [12]. It was shown by Kaaya [14,15] that the natural aging of PV modules can be described as the combination of three processes: hydrolysis, photodegradation and thermomechanical degradation. Module temperature is perhaps the most significant factor both due to its direct influence and also as a factor to increase the rate of other mechanisms. Significant differences are observed between the various cell technologies, as reported by Bansal et al. [3].

It has been broadly reported in the literature [16–18] that PV components are affected by critical failures with a broad range of frequency and performance impacts [19]. Conversely, in tropical climatic conditions, it has been observed that the degradation of I-V characteristics in PV modules differs. As an example, in Senegal, a PV module at mid-life demonstrated the highest decline in maximum power ( $P_{\max}$ ) ranging from 0.22% to 2.96% per yr, while its open-circuit voltage ( $V_{oc}$ ) remained unaffected [20]. Under desert conditions, the presence of cracked cells and other atypical physical material defects has been identified, leading to PV module degradation of up to 12% when compared to their initial performance [21]. It should be noted that the output power of crystalline-silicon solar panels is significantly affected by soil in desert regions [22]. For instance, under climatic conditions like in Saudi Arabia and Kuwait, soiling can cause a drop in the output power of up to 40% and around 65% respectively [23]. Previous studies have provided data indicating that dust accumulation on the surface of solar panels can result in efficiency reductions of 35% in the Bangladeshi environment [24] and 50% in the Malaysian climate [25].

Nonetheless, the causes of failures are very diverse and complex to anticipate. These could be classified into four main sources.

- **Environmental stress:** temperature, humidity, exposure to UV light, rain, and wind [26] as well as soiling, deterioration from animals and others. For instance, wires and electrical systems are particularly sensitive to wildlife intrusion from rodents, snakes and termites [27].
- **Poor quality during construction:** manufacturing, installation, transportation. Jordan et al. [6] highlighted that installation risks may be mitigated with proper training and inspections.

- **Unforeseen incidents from the design phase:** shading, significant potential differences leading to PID, lightning and more.
- **Accelerated aging:** fatigue, thermo-mechanical cycle, acetic acid formation in the encapsulant, material interactions and others.

At the level of individual PV modules, Aghaei et al. [11] showed the interconnection between failure causes and effects and highlighted the possibility of cascading failures such as the degradation of the encapsulant, which produces acetic acid and further accelerates degradation.

To mitigate PV failures, inspection methods enable to alert that the PV installation does not operate correctly [28]. In particular, each method detects a specific spectrum of failures according to its methodology and its detection perimeter [16,29]. Those methods can be defined by their maturity, cost and availability [28] and they can be categorized into three main categories:

- **Remote:** The detection is performed from automated readings according to sensors on the installation. The identification and classification of failures are then performed with data-driven methods [30].
- **In-situ:** The main tools include visual inspection, imaging methods, electrical protection testing and electrical testing [28]. It requires a specialist to go on-site and inspect the PV power plant. Those inspections usually provide a high level of precision on failure recognition, but involve some higher costs.
- **Laboratory tests:** Some detection methods such as lock-in thermography, require bringing PV modules to the laboratory for further tests. Those tests are excluded from the study scope since an operational methodology is envisioned and the logistics including plant interruption time, transportation, laboratory costs and so forth would make the inspection unrealistic in an operational setup.

Inspection methods and failures are closely intertwined. For instance, Figure 1 provides a summary of a set of 5 common inspection methods from a previous work [19] covering several literature sources [16,18,28] wherein the capacity to detect and identify module-level failures was assessed. Herein “detection” capability is defined as the ability to spot operating faults without pinpointing from which specific failures they originate. In contrast, “identification” precisely locates and thoroughly characterizes a fault. Remote techniques have high capabilities in detectability and sometimes even identifiability, which makes it a valuable tool in line with in-situ inspection techniques. However, these remote techniques are often less accurate at the module level where monitoring data are rarely collected and, the development of an in-situ protocol is key to identifying failures at this level.

The main objective of this article is to define and establish an in-situ protocol for the identification and diagnosis of failures of outdoor photovoltaic modules. This protocol encompasses a comprehensive methodology to detect the degradation modes using imaging techniques, electrical assessment, and a machine learning method to automate anomaly detection. The different methods featured in this protocol are visual inspection, infrared

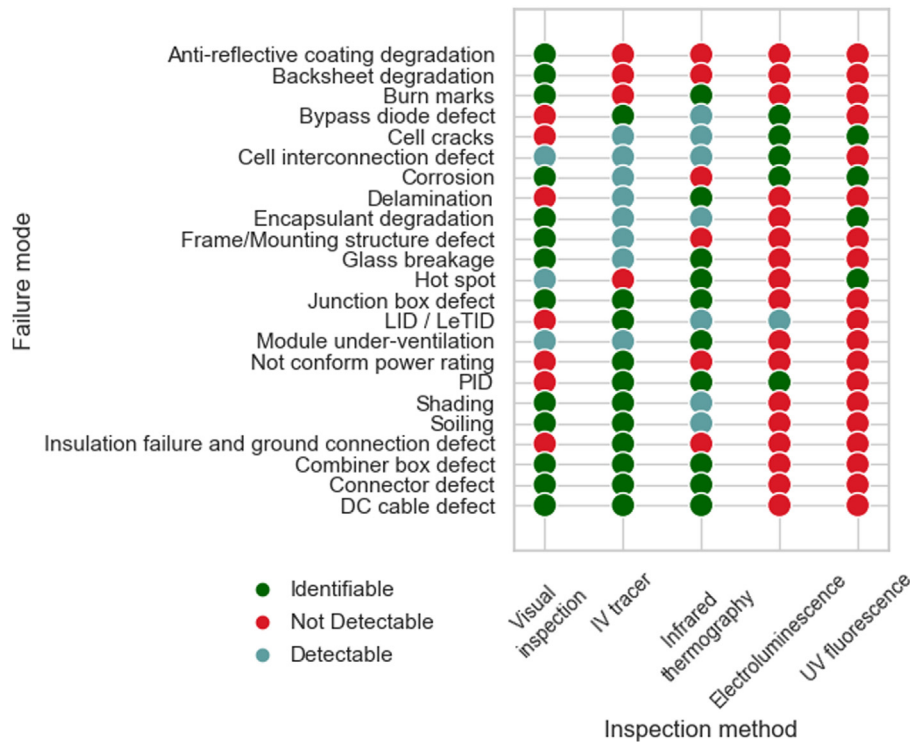


Fig. 1. Failure – detection capabilities correspondence on PV array.

imaging, ultraviolet fluorescence imaging (UVFL), electroluminescence imaging and I-V tracing. The protocol was further applied to the Djibouti PV installation, showcasing its ability to identify failures on a sample of 48 polycrystalline-silicon PV modules after 12 years of operation.

## 2 Methodology

### 2.1 Diagnosis technique

Various methods and tools exist for PV inspection without a clear consensus on which ones to employ and in what order to efficiently identify failures. As highlighted in the literature [19], there are a significant number of inspection methods with different coverages on the failure modes. This article primarily focuses on visual inspection, I-V curve tracing and imagery techniques as it covers the identification of most of the failure modes over the PV array, which could arise over the lifespan of the installation. Visual inspection, infrared imaging and I-V tracing are performed as the first steps since they allow to detect the widest range of failures. Then, some failures might remain unidentified and the high accuracy of the imagery methods (Electroluminescence and UV fluorescence) make it possible to precisely locate the failures.

### 2.2 Test site

A sample of 48 Kyocera KD210GH-2PU modules, forming a sub-array of a 302.4 kWp ground-mounted solar facility located in Djibouti was inspected using the various techniques described in the following section. The solar

facility is a grid-tied solar array that has operated continuously for 12 years. Located at the CERD, the solar array is monitored and manually cleaned on a daily to weekly basis. The 48 modules were all part of the original installation. The performance of the facility and the environmental context are described in previous works by the author [31,32]. A photograph of the facility is shown in Figure 2.

### 2.3 Failure mode detection protocol and measurement

In the current work, the PV module inspections comprised a combination of visual inspection, imaging techniques and electrical characterization. The approach followed a test protocol for outdoor PV failure diagnosis developed by the Laboratory of New and Renewable Energies of the Centre for Studies and Research (LENR-CERD).

#### 2.3.1 Overall protocol

The LENR-CERD test protocol is summarized in Figure 3. Modules are first cleaned to discard any heterogeneity from soiling. A visual inspection is then undertaken to develop a preliminary assessment of the array, followed up by infrared imaging to locate any temperature anomalies on the modules under operation. An analysis of the I-V curves is then undertaken to reveal the deterioration in the electrical characteristics. Finally, UVFL and EL are used to complete the inspection with further information regarding the nature of the faults. Lastly, the data is consolidated to construct a diagnostic of the module performance highlighting single-point failures.





**Fig. 2.** CERD solar facility.

The following instrumentation was used to undertake the protocol:

- FLIR E-6XT model for an infrared thermal imaging camera.
- Solmetric PV analyzer to assess the electrical characteristics of I-V data points [33].
- UVFL lamp.
- BrightSpot Automation 24 megapixel EL camera, plus a DC generator for electroluminescence imaging.

### 2.3.2 Visual inspection (VI)

Freshly cleaned modules are evaluated by visual inspection (VI). VI involves a thorough examination of the components and is an important step that can reveal several visible defects (bubbles, yellowing, delamination, snail trails, cell cracks, etc.) [11]. The result is a list of apparent problems that can be confirmed by subsequent measurements. This step also offers a first set of recommendations and insights for the following inspection steps.

### 2.3.3 Infrared (IR) imaging

Infrared thermography analysis provides a comprehensive understanding of the condition of the PV module by performing a non-invasive inspection method using infrared radiation (IR) imaging cameras. The main purpose of this technique is to evaluate the temperature distribution on the surface of the module, and especially to locate any hot spots on the photovoltaic module. The protocol recommends performing the IR inspection with the PV installation in operation under clear sky conditions between 9 AM to 10 AM with irradiance values higher than  $700 \text{ W/m}^2$  [34]. IR imaging can be strongly disrupted by direct solar radiation arriving on the panels when taking images at noon. Furthermore, prior to the IR imaging, the panels should be cleaned before taking the first images to avoid having inaccurate findings because of the presence of dust on the panels.

### 2.3.4 Electrical characteristics (I-V) curves

I-V curves offer a quantitative account of the PV strings or modules in terms of their electrical response. These curves particularly give insights into the characteristics of the string/module, including its maximum power point (MPP), open-circuit voltage ( $V_{oc}$ ), short-circuit current ( $I_{sc}$ ), and fill factor (FF). These data facilitate the diagnosis of performance issues and highlight any deviations from expected behavior, allowing for timely maintenance and troubleshooting.

In this study, the PV modules were compared to the specifications provided by the PV module manufacturer with an uncertainty of  $\pm 0.5\%$ . Along with the I-V measurement, the irradiance and cell temperature were measured according to the SolSensor with a typical uncertainty of 2% and  $2^\circ\text{C}$  respectively [33].

Correcting the I-V curves to Standard Test Conditions (STC  $1000 \text{ W/m}^2$ , module at  $25^\circ\text{C}$ ) is essential to evaluate the evolution of the module characteristics over time. To obtain the reference STC curve, the 5 parameters of the Single Diode Model (SDM) [35] ( $I_L, I_0, a, R_s, R_{sh}$ ) are fit according to the STC datasheet characteristics. The model further establishes the relationship between the module current  $I$  and the voltage  $V$  as shown in equation (1).

$$I = I_L - I_0 \cdot \left( \exp\left(\frac{V + I \cdot R_s}{a}\right) - 1 \right) - \frac{V + I \cdot R_s}{R_{sh}}. \quad (1)$$

Among the several methods [36,37] to translate curves to STC conditions, the correction procedure 1 from the standard IEC 60891-1 [38] has been followed.

$$I_2 = I_1 + I_{sc1} \cdot \left( \frac{G_2}{G_1} - 1 \right) + \alpha \cdot (T_2 - T_1), \quad (2)$$

$$V_2 = V_1 - R_s \cdot (I_2 - I_1) - k \cdot I_2 \cdot (T_2 - T_1) + \beta \cdot (T_2 - T_1). \quad (3)$$

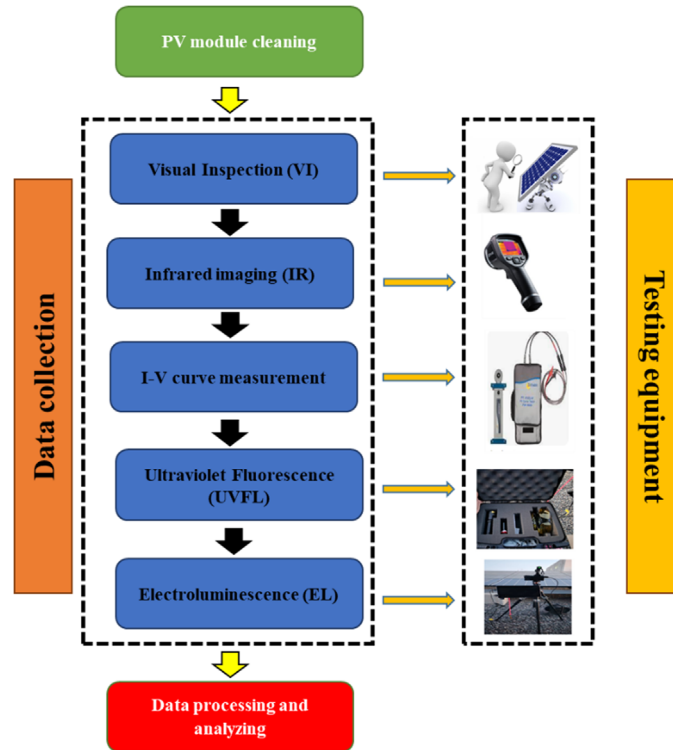


Fig. 3. Testing protocol.

$I_2$  and  $I_1$ ,  $V_2$  and  $V_0$ ,  $T_2$  and  $T_1$ , and,  $G_2$  and  $G_1$  are the current, voltage, module temperature, and irradiance after and before correction, respectively.  $I_{SC1}$  is the short-circuit current before correction.  $\alpha$  and  $\beta$  are the PV module absolute temperature coefficients at open-circuit and short-circuit respectively which are extracted from the manufacturer's datasheet. Then, the correction factor  $k$  and the internal resistance  $R_s$  are deducted from simulated curves thanks to the SDM with the method suggested by Li et al. [36,39] and are respectively equal to 0.0007 and 0.35  $\Omega$ .

All the 48 measured I-V curves were translated from the local environmental conditions to STC conditions. To achieve this correction, it is advisable to conduct measurements at irradiance levels over 700 W/m<sup>2</sup> according to the IEC standard 60891 [40]. I-V curves were collected with irradiance levels at not less than 950 W/m<sup>2</sup> over the 48 module measurements spanning from 11 to 12 (GMT+3) on 27 February 2024. I-V measurements were done with a Solmetric I-V curve tracer by isolating each module from the rest of the installation. More details regarding I-V characteristic measurement and test protocol can be found in our previous work [34].

### 2.3.5 UV fluorescence (UVFL) imaging

Electroluminescence and UVFL are made in dark environments such as in a dark room for indoor tests or at nighttime for outdoor tests. UVFL is a characterization method that allows detailed inspection of encapsulation materials in photovoltaic modules. This imaging technique can detect several failures occurring in the lifetime of the PV module like discoloration, delamination, snail trail, cell

cracks, hot spots and more. The UVFL imaging was performed at nighttime with a UV lamp with an emission spectrum of 350 nm [41].

### 2.3.6 Electroluminescence (EL) imaging

EL imaging is based on the physical phenomenon of electroluminescence, whereby a material emits light when stimulated electrically. Under DC excitation, c-Si photovoltaic cells emit infrared radiation (IR) with a wavelength of 1000–1300 nm and a peak value of 1150 nm, and its intensity depends on the bias voltage of the cell. EL imaging can identify local cell failures as well as inhomogeneities within the module [42]. Electroluminescence imaging was performed using a BrightSpot Automation 24 megapixel EL camera and a DC generator connected to the PV module under test. The electrical parameters of the generator are set according to the PV module under test ( $I_{SC}$  = 8.56 A and  $V_{OC}$  = 33.2 V). The voltage of the power supply should be set at 10% higher than the  $V_{OC}$  ( $V$  = 36.5 V). All are connected to a tablet with an IMPEL software for camera control and, image visualization and processing.

## 2.4 Analysis of thermal imaging data

Knowing that there are several artificial intelligence (AI) methodologies and models [43–47] used in image classification, the choice of the method depends on the specific requirements of the task, such as the need for high accuracy, computational efficiency, training dataset availability, etc. For this purpose, the IR images were inspected

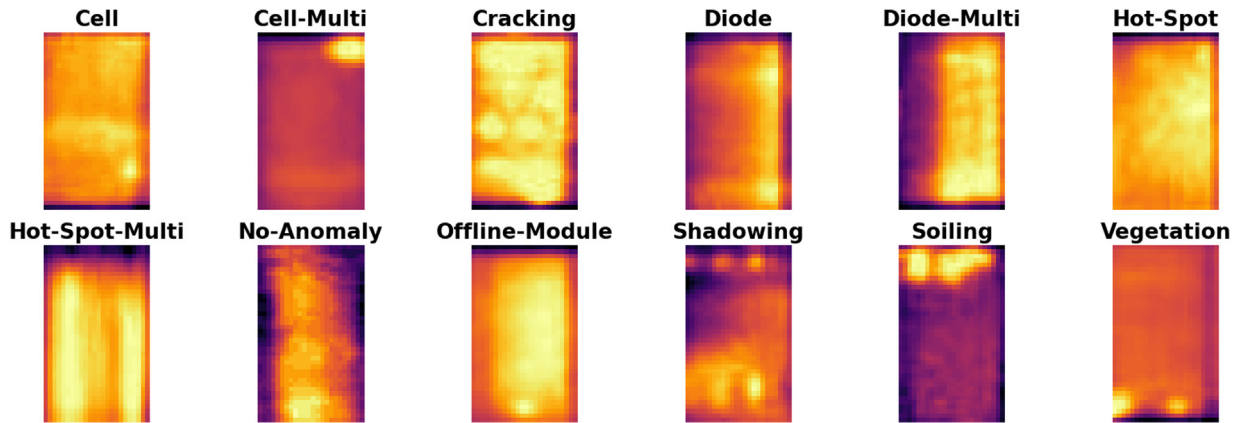


Fig. 4. Samples obtained from each dataset of “InfraredSolarModules”.

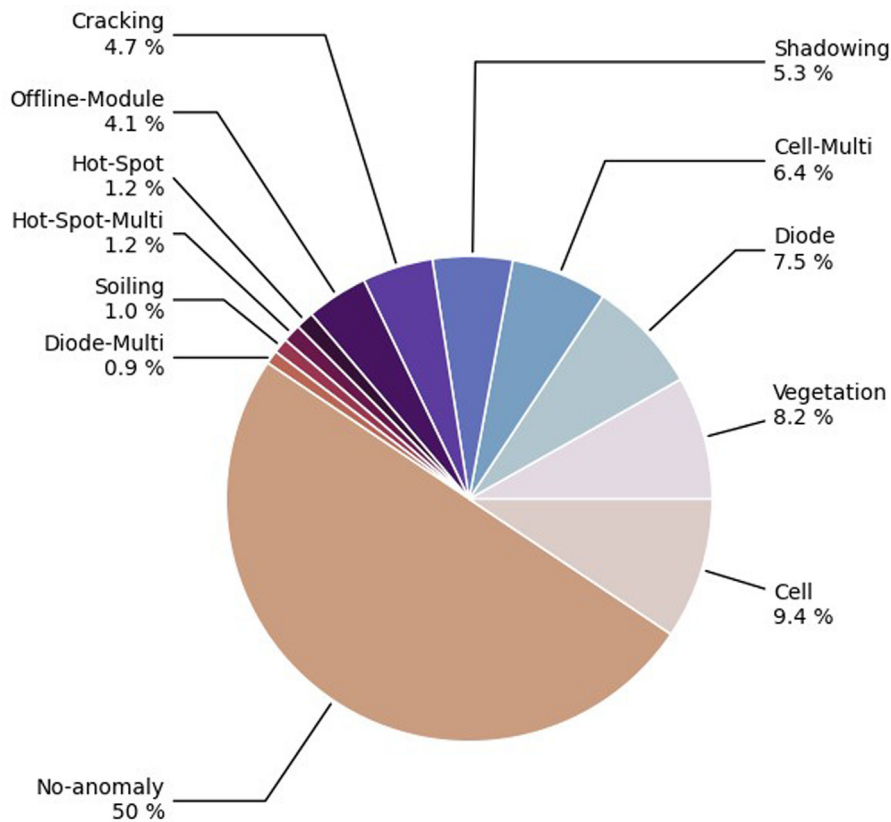


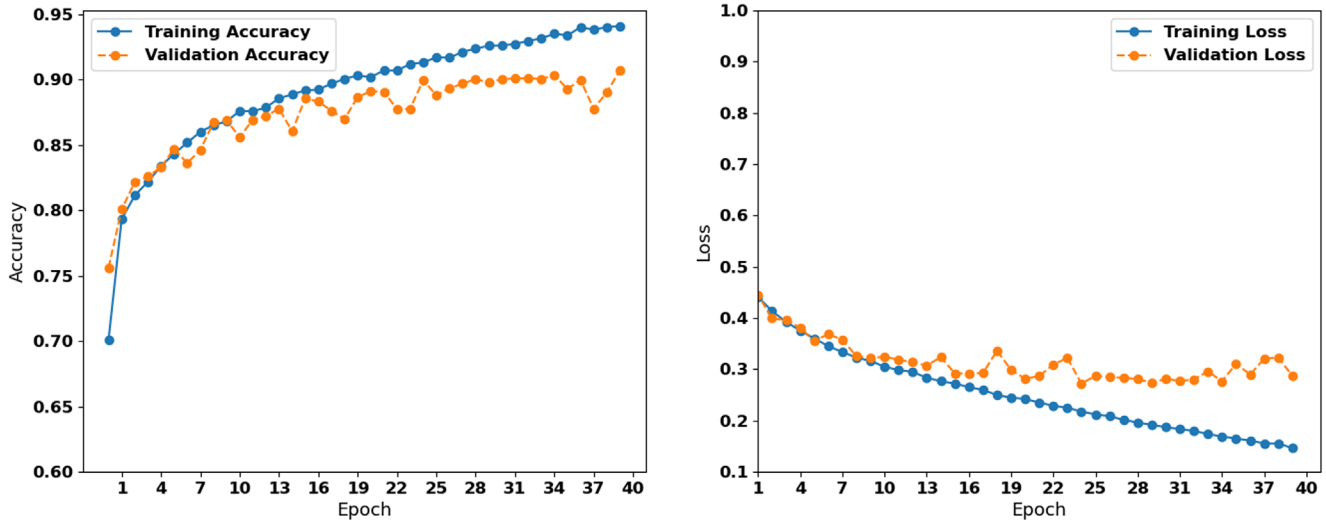
Fig. 5. Proportions for each of the 12 classes.

automatically for fault signatures with the aid of the Convolutional Neural Network (CNN) model. In order to train the CNN, a reference dataset was utilized: the “InfraredSolarModules” dataset, publicly available under a MIT license. This dataset comprises thermal images of PV modules, capturing various anomalies. It was meticulously collected, annotated, and structured by Millendorf et al. [43]. The dataset encompasses 20,000 thermal images, categorized into eleven distinct anomaly classes (10,000) and one class with no anomaly (10,000 images). Figure 4 presents the twelve different classes.

In Figure 5, the proportions are depicted for each of the eleven anomaly classes, as well as the class denoting the absence of anomalies. It illustrates that the dataset exhibits an imbalanced distribution, reflecting the real-world prevalence of PV anomalies. Unbalanced datasets possess the potential to exert a significant influence on the training process of neural networks, thereby influencing their ability to effectively generalize the minority of samples. There are several methods to address this issue; however, in our case, we employed the “under-sampling” method, which means reducing the size of the majority class by randomly removing samples.

**Table 1.** Dataset groups EG and TG.

Estimation group (85%)		Testing group (15%)	Total number of images (100%)
Training set	Validation set	Testing set	
14 750	2 250	3 000	20 000

**Fig. 6.** Evolution of the CNN model training and validation accuracy (a) and loss (b) for 40 epochs.

The methodology proposed in this work aims to address two different scenarios, as suggested below.

#### 2.4.1 First step: detection of fault in PV module

The initial step involved implementing a Convolutional Neural Network (CNN) to analyze a set of IR images. The objective is to determine whether a given solar panel exhibits any defects or no anomalies. To carry out this analysis, the dataset was divided into two main groups: an Estimation Group (EG) comprising 85% of the images and a Testing Group (TG) containing the remaining 15% (Tab. 1). Both groups were selected randomly, ensuring a consistent distribution of each class for training purposes. Within the EG, a further division occurred, creating distinct subsets for training and validation. The TG, on the other hand, was utilized exclusively after the validation of the training process. This segregation ensured that the testing phase was only initiated once the network had been adequately validated. Consequently, post training, the ability of the network to generalize on unseen data was evaluated. The primary objective was to determine whether the CNN could effectively identify defects in images sourced from other PV plants, establishing its potential applicability beyond the initial training dataset.

In order to do this, a CNN using a Nadam optimizer, a 0.001 learning rate, 32 samples as batch size, and training time given by 40 epochs were used as parameters for the CNN model. The evolution of the accuracy of the proposed model, considering both the training and validation accuracy is shown in Figure 6a. As observed, the training

accuracy curve increases as the model learns from the data. At the end of the training, the model presented a 94.64% accuracy in the training set, 90.19% in the validation set, and 89.73% in the previously unseen data during the testing phase.

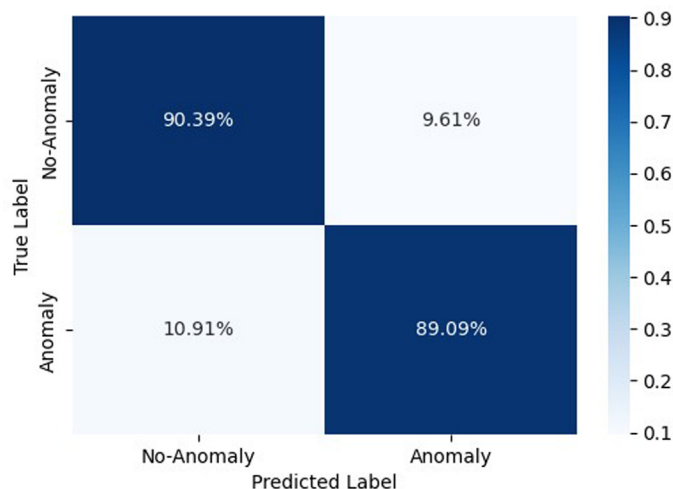
Figure 6b shows the evolution of the loss function of the proposed model taking into account the training and validation loss. The training loss curve represents the prediction error on the training data, and a decrease in this curve indicates that the model is learning from the training data. Similarly, the validation loss curve displays the loss on unseen data, resulting in a decrease indicating a good performance on the data. It took about 34 epochs for the validation loss to start stabilizing. Continuing to run the network for additional epochs resulted in an increase in the validation loss, indicating overfitting to the training set.

A predictive analytic technique called a confusion matrix is used to describe how well a deep learning classification model performs. The confusion matrix of the trained model in the test set is illustrated in Figure 7. The matrix reveals that the model achieved an accuracy of 90.39% in classifying instances without anomalies (no-anomaly class) and achieved an 89.09% accuracy in identifying solar modules with defects.

#### 2.4.2 Second step: classification of anomalies in PV modules using the “under-sampling” method

The second scenario implied the creation of a classifier for eleven potential defects in PV modules through the under-sampling of the “InfraredSolarModules” Dataset. In this





**Fig. 7.** The confusion matrix obtained during the first scenario.

approach, all classes were downsized to match the size of the smallest class, which is “Diode-Multi”. Accordingly, 175 images from each of the eleven classes were randomly selected, resulting in a balanced dataset comprising 1,925 defective thermographic images. Due to the limited amount of data available for each class, a ten-fold cross-validation process was implemented. In this scenario, the 1,925 IR images were divided into 5 folds of 192 IR images and 5 folds of 193 IR images. Each fold maintained a proportional representation of all eleven different classes of PV faults. This ten-fold approach aimed to ensure robust evaluation and validation of the classifier performance across the diverse set of defects in the PV modules. Table 2 presents the main results of training and testing for each of the ten-fold training cases. At the end of the training, the average testing accuracy was 87.6%, and the best case was given by the 8th fold with a testing accuracy of 95.31%.

Figure 8 shows the confusion matrix of the trained model for all the ten folds of the second scenario. Knowing that the diagonal elements represent the correct predictions, off-diagonal elements indicate the misclassifications. The matrix is generally diagonally dominant, denoting good performance, as the main diagonal has higher values than the off-diagonal ones. As shown in the confusion matrix, the model seems to perform well overall as the main diagonal has elevated values, specifying that the model is making correct predictions for most of the classes.

## 3 Results and discussion

### 3.1 Visual inspection

During the visual inspection, numerous defects were discovered, including encapsulant discoloration, snail trails and backsheet bubbling. A detailed description of the visual inspection results is shown in Table 3. A summary of the statistical analysis and evaluation of the degradation of the PV system component is displayed in Figure 9. Encapsulant discoloration was observed to be the most

common degradation mode in all PV modules. It was followed by backsheet bubbling and snail trails, which occurred in 45 over 48 modules (93.7%) and 2.1% of the cases respectively.

### 3.2 Infrared imaging

The observed defects on visual inspection were thoroughly analyzed through infrared thermography with the PV installation in operation. Figure 10 shows the infrared images of the front and rear sides of a module presenting bubbles. By analyzing these IR images (Fig. 10a), the exact location and the accurate size of the bubbles can be discerned. They are discernible and indicated by a greenish coloration. Based on the temperature gradient displayed in the image, the areas affected by this degradation had a lower apparent temperature than the rest of the backsheet, of around 50°C. On the front side, the infrared image indicated the presence of hotspots at an apparent temperature of 50.9°C (Fig. 10b) on certain cells according to the hot spot detection algorithm. These cells were precisely located where the bubbles were situated.

Figure 11 shows the IR images of a module presenting several snail trails. Multiple cells were found to exhibit relatively high temperatures with differences of 5 to 6°C. Indeed, hot spots were expected to be associated with snail trails since they are known to have a detrimental impact on the performance of PV modules and may serve as an indicator of moisture ingress, often attributed to mechanical stress resulting from the loss of module hermeticity and cell cracking.

One of the key findings from the IR imaging analysis was that all solar cells located directly on top of the junction boxes were approximately hotter than the other cells with a temperature difference from 8°C to 13°C (Fig. 12). On the rear side of the PV module, it could be noticed that the temperature of the junction box was extremely elevated as high as 63.7°C. This indicated that more cell thermal stress may have occurred at these locations and as a result led to hot spots [48]. A higher temperature was observed when the bypass diode inside the junction box was activated.

The importance of employing infrared imaging techniques in this context becomes evident as it demonstrated that the detected hot spots may have had several underlying causes that justified their presence. This underscored the significance and relevance of utilizing infrared imaging to further elucidate the observed degradation modes during visual inspection. However, to determine the underlying reasons that these hot spots were indicated, we will delve deeper with I-V characterization, UVFL and EL imaging, which will give us more insights into the state and performance of the modules in question.

### 3.3 I-V characterization

From an electrical perspective, I-V curves were collected over the 48 modules and translated to Standard Test Conditions (STC) with the methodology explained earlier in Section 2.3.4. All the characteristic points ( $I_{sc}$ ,  $V_{oc}$ ,  $I_{mpp}$ ,

**Table 2.** 10-fold cross-validation performed on a dataset of 2,100 images to classify between 11 different defects.

$k$ - fold	Training loss	Training accuracy	Testing loss	Testing accuracy
Fold 1	0.215	0.930	2.819	0.497
Fold 2	0.056	0.985	0.965	0.814
Fold 3	0.055	0.982	0.203	0.948
Fold 4	0.058	0.984	0.535	0.933
Fold 5	0.042	0.986	0.945	0.928
Fold 6	0.043	0.989	0.514	0.938
Fold 7	0.026	0.992	0.874	0.917
Fold 8	0.022	0.994	0.394	0.953
Fold 9	0.028	0.993	0.928	0.917
Fold 10	0.066	0.985	0.968	0.917

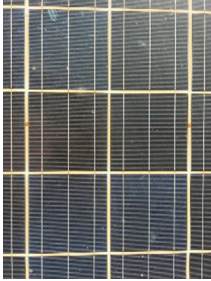

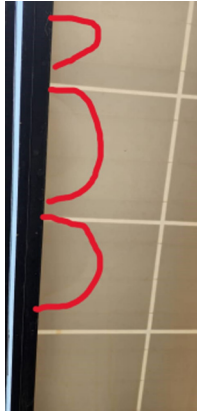
**Fig. 8.** The confusion matrix from the tenth fold of the second scenario.

$V_{mpp}$ , FF) were extracted from the I-V curves as shown in Figure 13 and were compared to the initial STC manufacturer datasheet values.  $I_{sc}$  corresponds to the short-circuit current and  $V_{oc}$  is the open-circuit voltage. The current and voltage at the maximum power point (MPP) are denoted  $I_{mpp}$  and  $V_{mpp}$ . The Fill Factor (FF) corresponds to the ratio of  $I_{mpp}$  and  $V_{mpp}$  product at MPP and the product of  $I_{sc}$  and  $V_{mpp}$ . Moreover, the resistance in series  $R_s$  and parallel  $R_{sh}$

which are equal to the inverse of the slope at the open-circuit and short-circuit points respectively are qualitatively evaluated for some of the modules.

For almost all the tested modules, a decrease in all the studied characteristics was observed compared to the initial assumed datasheet STC values. The evolution of each electrical characteristic is shown in Figure 14 and Table 4.

**Table 3.** Results of the visual inspection.

PV module components	Observation and remarks	Images
Front side Discoloration	EVA discoloration affects all the PV modules, with varying degrees of severity. It is uniformly widespread over all the cells of the panel. This alteration affects the transmittance of light reaching the solar cells, therefore leading to a reduction in power generation.	
Snail trails	Several snail trails are observed on one PV panel. It appears as a gray/black discoloration on the silver paste of screen-printed front metallization of solar cells. Snail trails observed on this panel vary in shape, color, and size. On two cells of this module, the snail trail is quite visible and thick, and spread across these cells.	
Rear side Bubbles	45 of the 48 PV panels exhibit bubbles on the rear-side. Some modules may contain multiple bubbles arranged side by side, each varying in size. These bubbles create an air chamber in which the gas temperature is lower than that in the adjacent cells. Bubbles have the potential to rupture, thereby causing damage to the rear sealing surface, hence facilitating the ingress of humidity. It represents a recurring form of degradation within this array, predominantly manifesting in the modules after years of operation.	

From [Figure 14](#), it can be observed that the characteristic points at the axis-intercepts with  $I_{sc}$  and  $V_{oc}$  were moderately impacted with a median decreasing by not more than 2%. The decrease at the operating points  $I_{mpp}$  and  $V_{mpp}$  had a wider distribution, but also exhibited a higher degradation with medians over 2%. The Fill Factor (FF) decreased within a range of 4.6% to 1.6% testifying for degradation on the resistance in series and in parallel. Overall, all the modules showed a decrease in STC power after 12 years of operation with a median reaching 5.5% corresponding to an average degradation rate of 0.46%/year which was well in line with silicon technology rates found in the literature [8,49].

Upon closer inspection, some I-V curves were found to contain several degradation features. This is illustrated in [Figure 15](#), which shows a module exhibiting increased slopes at the  $V_{oc}$  intersection from all measured I-V curves. The more pronounced slopes are a feature of the

degradation of the resistance in series  $R_s$ , which can typically increase when the electrical circuit is deteriorated caused by, for instance, a higher corrosion level due to aging mechanisms. It must be noted that the measured I-V curves do not attain the  $V_{oc}$  due to the STC translation which shifts the curve to account for the temperature difference between the measurement and the STC conditions.

Then, when zooming on the section between 5 V and 25 V in [Figure 15](#), the slopes from modules 40 and 42 are sensibly smooth and almost parallel to the STC curve, but not for modules 4 and 13. For the latter two modules, a cascade of steps decreasing the current at around 7.5 V–8 V intervals indicates some mismatches in the current generation between the three cell strings, which are separated with bypass diodes in the module. This mismatch between the three cell strings is more clearly identified in [Figure 16](#) on module 13 where each cell string has a distinctive maximum current level. These mismatches are typical when the module

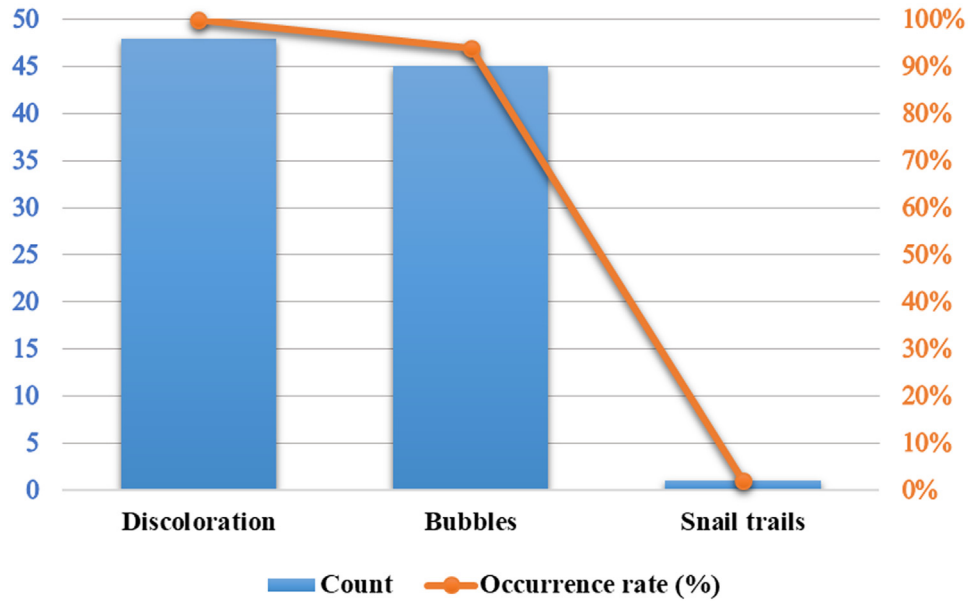


Fig. 9. Frequency count and occurrence of observed degradation during visual inspection.

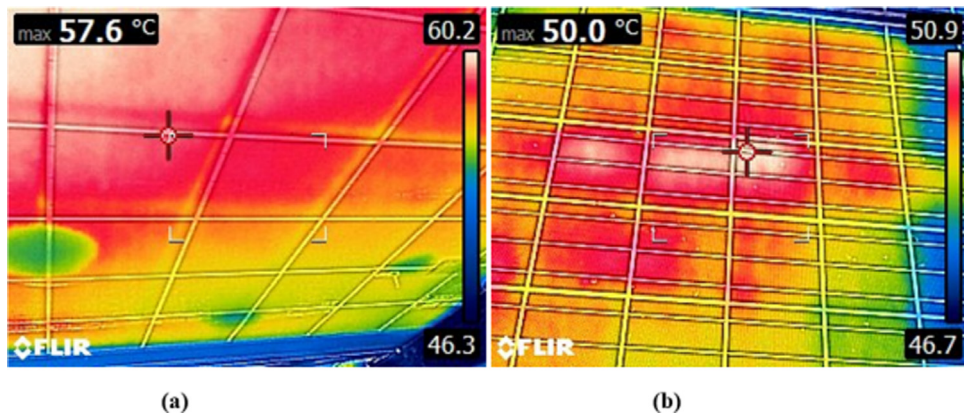


Fig. 10. Infrared images of bubbles on a PV module viewed on the backside (a) and on the front side (b).

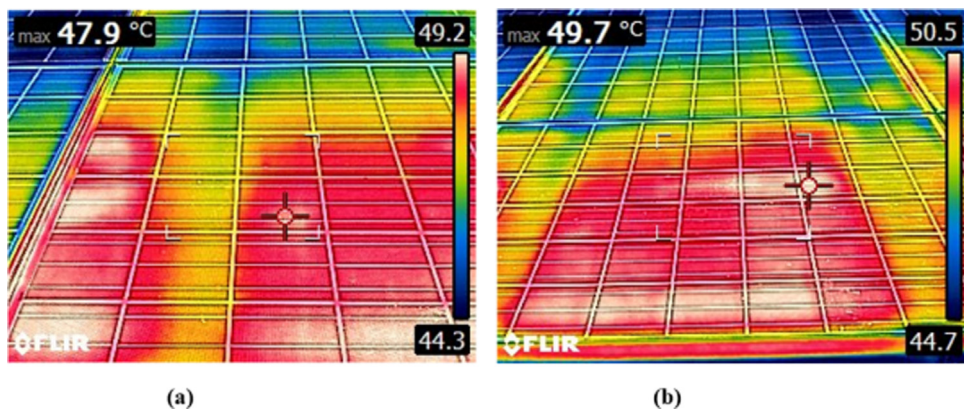


Fig. 11. Infrared images of snail trails on a PV module viewed on the edges (a) and on the center (b).



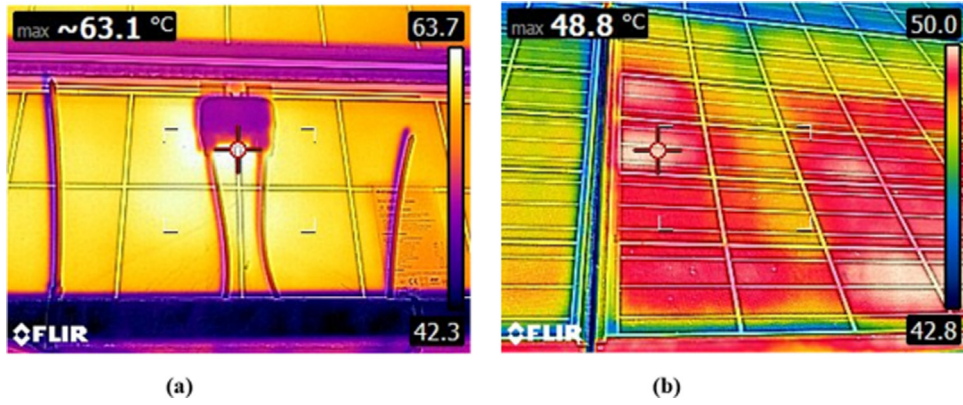


Fig. 12. Infrared images of the junction box of a PV module on the backside (a) and on the front side (b).

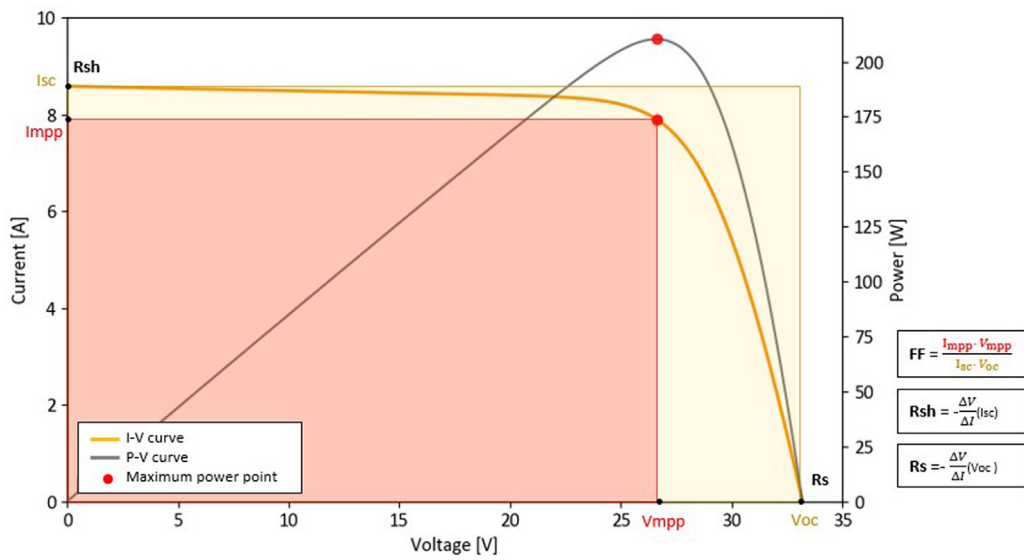


Fig. 13. Illustration of the characteristic I-V points with the Kyocera KD210GH-2PU module I-V curve at STC conditions.

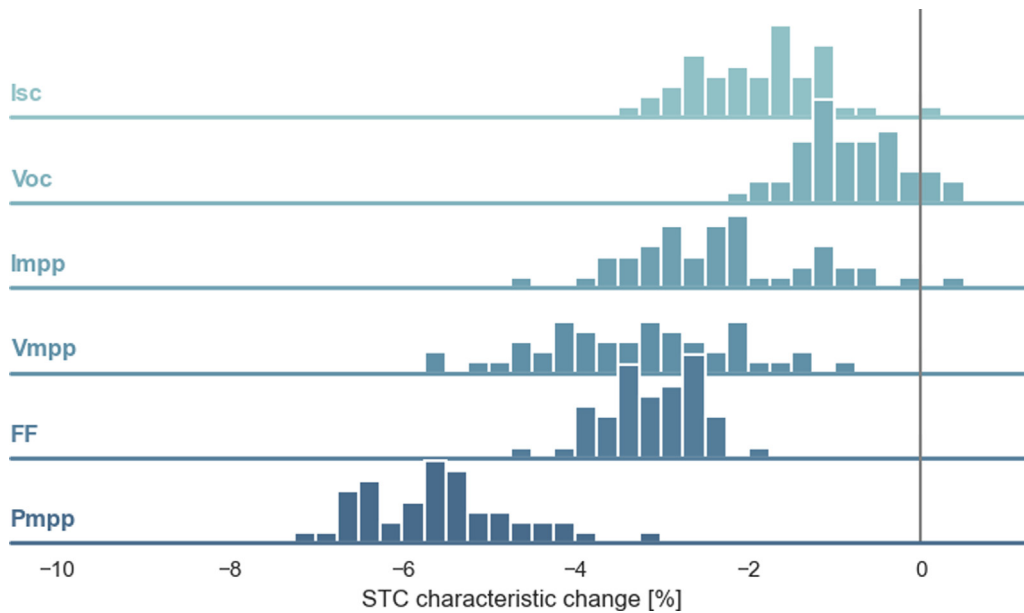
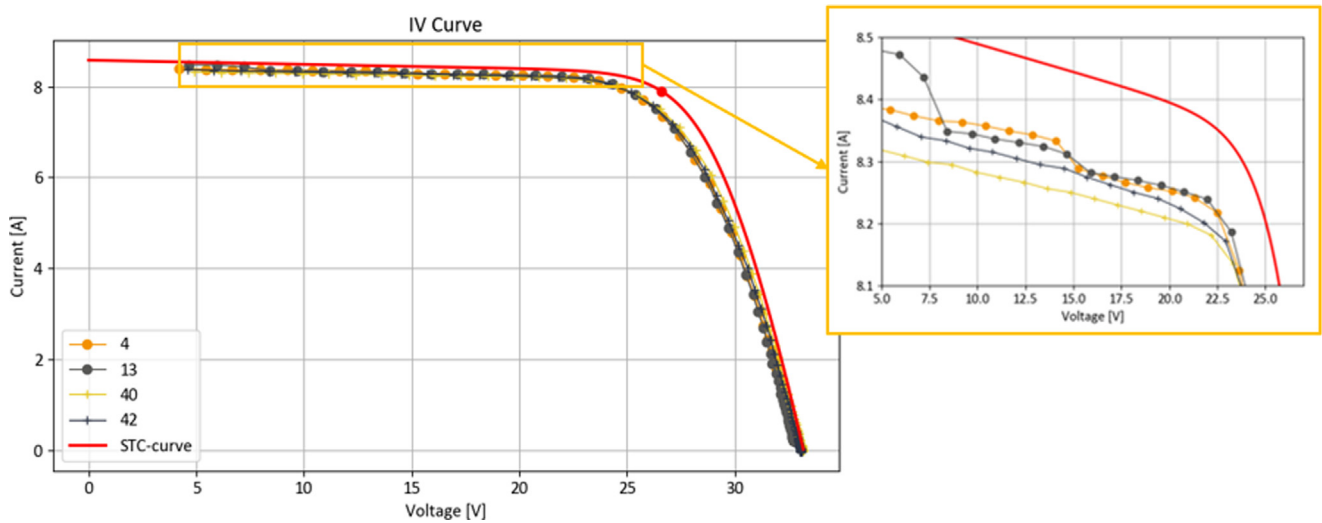
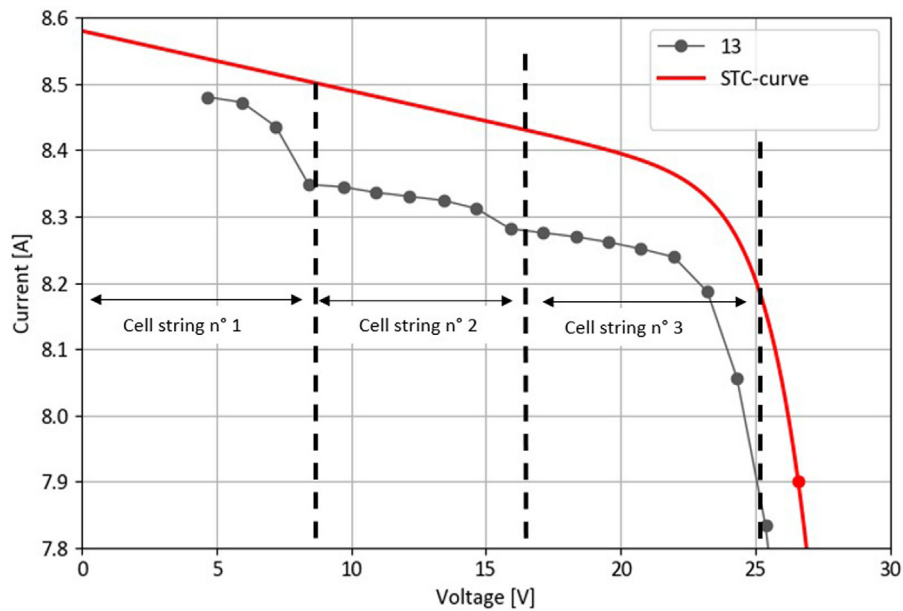


Fig. 14. I-V characteristic degradation after 12 yr of operation on a population of 48 modules.

**Table 4.** I-V characteristic degradation statistics over the 48 studied modules.

	STC reference	Median over the module population (#48)	Lower/upper bounds over the module population (#48)
$I_{sc}$ [A]	8.58	8.43 (-1.7%)	[8.3, 8.58] (-3.3%, 0.0%)
$V_{oc}$ [V]	33.2	32.9 (-0.9%)	[32.53, 33.36] (-2.0%, 0.5%)
$I_{mpp}$ [A]	7.9	7.71 (-2.4%)	[7.54, 7.92] (-4.6%, 0.3%)
$V_{mpp}$ [V]	26.6	25.73 (-3.3%)	[25.08, 26.34] (-5.7%, -1.0%)
FF [%]	73.77	71.67 (-2.8%)	[70.48, 72.62] (-4.5%, -1.6%)
$P_{mpp}$ [W]	210	198.39 (-5.5%)	[195.17, 203.76] (-7.1%, -3.0%)

**Fig. 15.** I-V curves of the PV modules 4, 13, 40, 42 with the initial STC curve (red).**Fig. 16.** I-V curve of the PV module 13 with the initial STC curve (red).

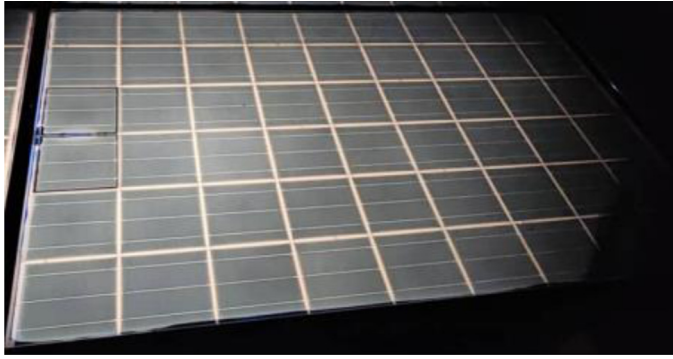


Fig. 17. UVFL image of a PV module.

integrity is compromised due to cell-micro-cracks, delamination, EVA deteriorations, etc., that are most often correlated to hot spots, as observed with the other inspection methods.

After 12 years, it was shown that the STC power degradation over all the 48 sampled modules had a distribution ranging from 3% to 7.1% with a median of 5.5% corresponding to a yearly degradation rate of 0.46%/yr. Even though the degradation remained moderate, this analysis particularly sheds light on the presence of degradations of resistances in series and microcracks, which might have accentuated hot spot effects and led to some accelerated aging of the PV modules in the long term.

### 3.4 UV fluorescence (UVFL) imaging

In Figure 17, dark streaks are clearly visible in UVFL images of PV modules, located in the junction boxes. These dark streaks may potentially be attributed to the accumulation of contaminants such as dirt or dust in the vicinity of the cells adjacent to the junction boxes. Moreover, it was observed through infrared imaging that the areas where the cells or junction boxes were situated exhibited high temperatures in comparison to the remaining cells of the module, occasionally manifesting as 'hot spots'. Despite the absence of visible evidence during visual inspections, it is evident that the utilization of UVFL corroborates the outcomes obtained through the infrared imaging technique.

Following the utilization of three distinct inspection techniques, and being aware of the outcome of each approach, the UV fluorescence method was ultimately implemented as an evaluative tool for photovoltaic modules. Commencing with the solar panels that underwent visual examination, with a focus on the presence of snail trails, the image in Figure 18 was obtained.

Snail trails are a phenomenon that is primarily seen in c-Si PV modules after several months to a few years of operation in the field, as shown in Figure 18. The UVFL method, as depicted in Figure 19a, proves to be a more effective means of detecting this phenomenon. Areas on the surface of the PV panel affected by snail trails contain substances or contaminants exhibiting distinct fluorescence properties compared to the surrounding regions.

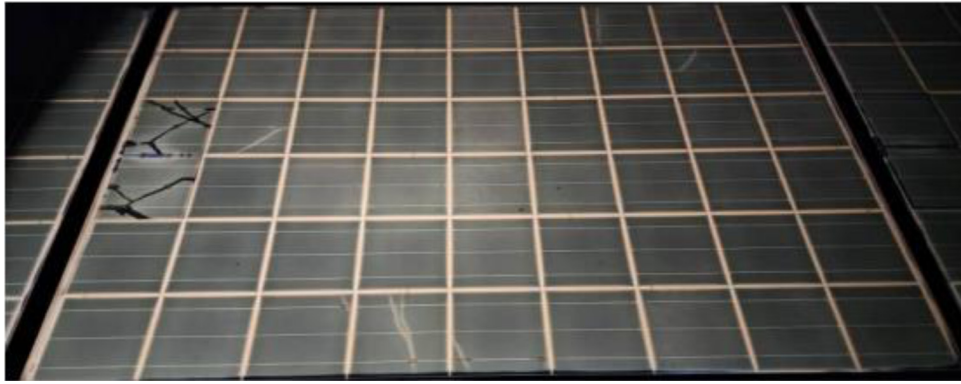
This discrepancy results in the manifestation of dark streaks or lines when observed under UV fluorescence. Nevertheless, both visual inspection and Infrared imaging techniques are also useful in identifying snail trails over an extended post-installation period. It is important to understand that snail trails have a negative effect on the performance of the PV module and can be used as a sign of moisture infiltration. This is frequently due to mechanical stress brought on by the loss of module hermeticity and cell breaking. This is discernible in UVFL imaging. Figure 19b illustrates cracks in four different cells on the PV module. These cracks can disrupt the electrical conductivity within the affected cell regions, resulting in a decrease in short-circuit current, an increase in series resistance, and thereby, in a reduction in the output power of the PV modules and, by extension, the entire PV array.

### 3.5 Electroluminescence imaging of field-installed PV modules

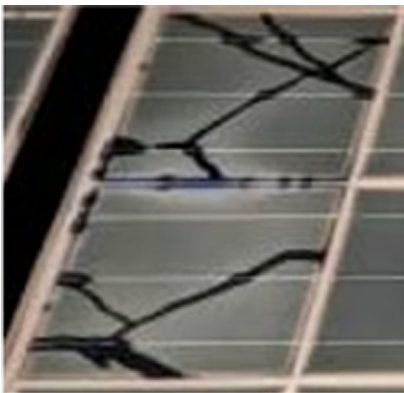
EL imaging technique enables a comprehensive understanding of PV module degradation modes. Therefore, EL analysis was conducted on field installed PV modules. To achieve this, the panel containing the snail trails for visual inspection was selected. A DC power supply was employed to pass a current equal to the rated short-circuit current of the module so as to achieve the forward biasing of the module. EL images were captured with an exposure duration of 10 seconds. Notably, since the modules within the site are affixed to the support structure, EL images obtained during the survey exhibit modules with a parallel orientation mounted on the structure. As depicted in Figure 20, the extent of cracks within the module becomes readily discernible in these images.

Figures 21a and 21b show material flaws that resulted from the production process, most notably finger interruptions. Unless they are caused by significant mechanical strain at the solder joints, these specific abnormalities normally do not shorten the operational lifespan of the involved solar panel. EL images reveal the presence of cracks in several modules. These cracks have been categorized into three groups, based on the extent of the affected area, as demonstrated in the EL image captured at the short circuit current, as depicted in Figure 22: (a) Mode A – hairline cracks, without any dark area (b) Mode B – cracks associated with grey areas in the cell (c) Mode C – cracks associated with dark areas in the cell. Mode A cracks are typically regarded as harmless and do not impact the power generation of the modules. On the other hand, the dark regions associated with Mode B and Mode C cracks can result in power loss. This is because dark areas in electroluminescence images signify a disruption in the electrical connection to the affected region, thereby influencing the efficiency of the cell and the overall power output of the photovoltaic panel.

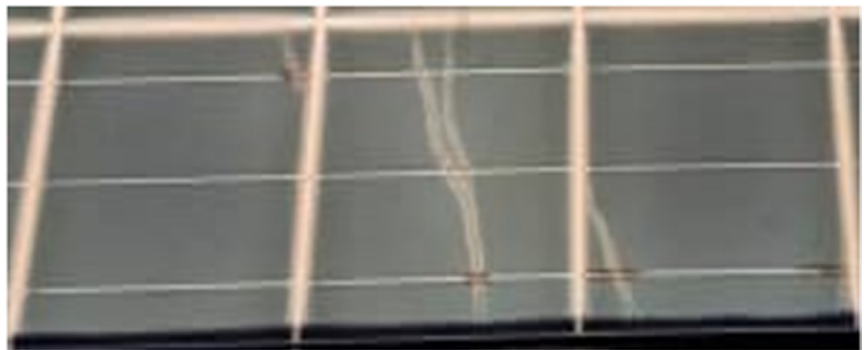
Finally, it is evident that a correlation exists among various inspection methods employed to ascertain the deteriorations affecting a panel. For instance, on a single panel, the presence of snail trails was observed. Subsequently, when employing infrared imaging, it was



**Fig. 18.** UVFL image of a PV module affected by snail trails.

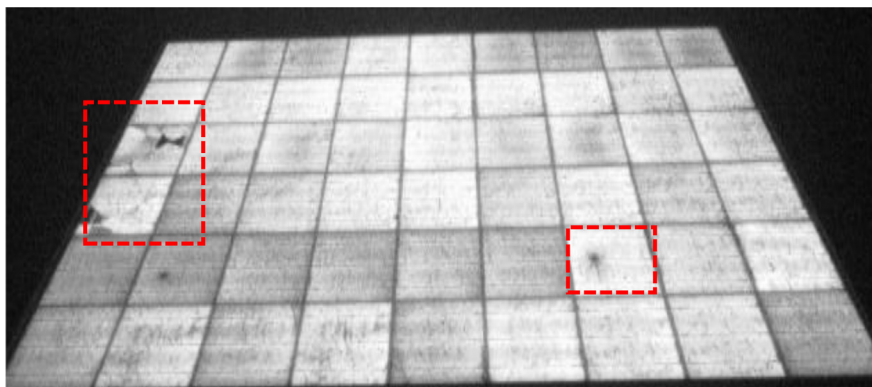


**(a) Snails trails**



**(b) Microcracks**

**Fig. 19.** UVFL image of a PV module: (a) affected by snail trails and (b) affected by microcracks.



**Fig. 20.** EL images for 54 cells of a polycrystalline module.

discerned that these snail trails manifested as hot spots. The presence of the latter can be attributed to multiple potential causes. Ultimately, electroluminescence allowed us to pinpoint the exact cause of these snail trails, which is a broken cell that can potentially impact the overall output power of the PV panel. EL imaging technique can provide a deeper understanding of the situation and precisely identify the source of the problem. Comparing the three imaging techniques, it is possible to identify a

connection among visual defects, hot areas, and electrically isolated regions. In summary, it is deducible that this embodies a progression of occurrences aimed at systematically identifying the type of degradation, drawing upon a variety of inspection methods to guarantee precision. Furthermore, in the following section, CNN techniques will be applied to automatically detect and classify the observed failures in the IR images from the array under inspection.



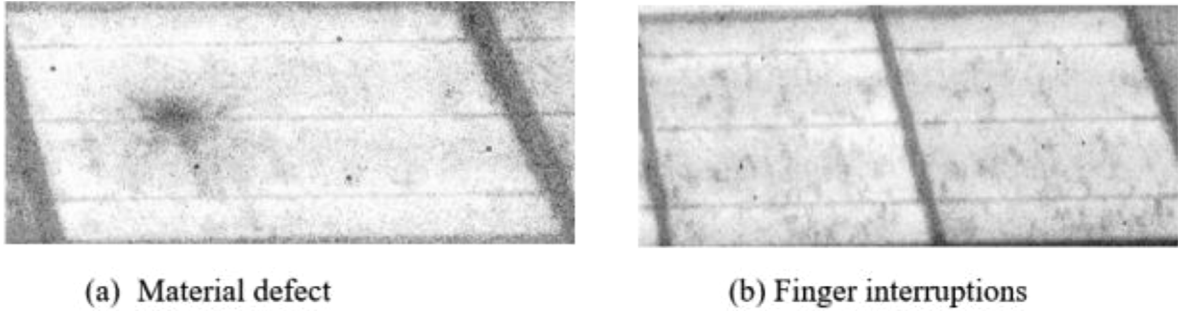


Fig. 21. Defects on solar cells.

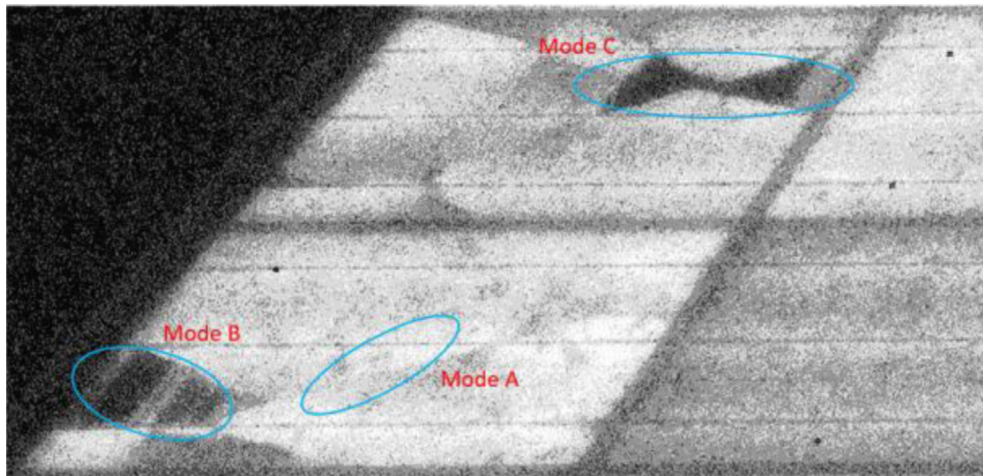


Fig. 22. Different types of cracks as visible in EL images.

Image: 1560.jpg, Predicted Class: Cracking  
 Image: 28.jpg, Predicted Class: Offline-Module  
 Image: 29.jpg, Predicted Class: Offline-Module  
 Image: 65.jpg, Predicted Class: Offline-Module  
 Image: 66.jpg, Predicted Class: Offline-Module  
 Image: 7923.jpg, Predicted Class: Hot-Spot  
 Image: FLIR0038.jpg, Predicted Class: Shadowing  
 Image: FLIR0039.jpg, Predicted Class: Shadowing  
 Image: FLIR0040.jpg, Predicted Class: Cracking  
 Image: FLIR0041.jpg, Predicted Class: Diode-Multi  
 Image: FLIR0043.jpg, Predicted Class: Cell-Multi  
 Image: FLIR0045.jpg, Predicted Class: Shadowing  
 Image: FLIR0046.jpg, Predicted Class: Cell  
 Image: FLIR0047.jpg, Predicted Class: Shadowing  
 Image: FLIR0048.jpg, Predicted Class: Cell-Multi  
 Image: FLIR0049.jpg, Predicted Class: Cell-Multi

Fig. 23. Predicted classes by the CNN model.

### 3.6 Convolutional neural network (CNN)

This section investigates the PV anomaly detection and classification via Convolutional Neural Network (CNN).

After training the model on the “InfraredSolarModules” dataset, IR images from our photovoltaic field were introduced into the model. These images were initially resized to match the sample size, and subsequently, the model permitted to classify them based on their respective defects. The ensuing responses are shown in Figure 23.

Firstly, it should be noted that the images of defects proposed to the CNN were already manually catalogued. Next, it was observed that the CNN model had correctly predicted the majority of images, which aligns with what had been deduced from the results of the confusion matrix. However, there are two instances of inaccuracies in the predictions made by the CNN model, specifically, for the images labeled FLIR0045 and FLIR0047, the predicted classification should correspond to the “Hot-Spot-Multi” category.

In summary, it can be concluded that the CNN model performs well. Therefore, it would be interesting to use this model for predicting future infrared images taken from the photovoltaic field instead of classifying them manually one by one. This would represent a time-saving benefit.

## 4 Conclusion

Failure mode detection and diagnosis were undertaken for a sample of 48 multicrystalline-silicon PV modules after 12 years of operation in a ground-mounted solar array in Djibouti. A test protocol was introduced for this assessment, comprising a combination of imaging techniques (visual inspection, infrared thermography, ultraviolet fluorescence and electroluminescence) plus electrical characterization. A convolutional neural network (CNN) model was used for the identification of features in the PV module images. Based on the study, the following conclusions have been drawn:

- Visual inspection revealed significant encapsulant discoloration as the most common degradation feature across the sample of PV modules, followed by backsheet bubbling and the presence of snail trails on 45 and 1 out of 48 modules, respectively.
- Infrared imaging was proven essential to associate the presence of hot spots with visible snail trail features, and overall to reveal sites of significant thermal stress, a process that was shown to be effectively automated thanks to a trained CNN model.
- The average decrease percentage of the 48 PV modules are 1.7%, 0.9%, 2.4%, 3.3%, 2.8% and 5.5% for  $I_{sc}$ ,  $V_{oc}$ ,  $I_{mpp}$ ,  $V_{mpp}$ , FF and  $P_{mpp}$  respectively.
- The combination of UV fluorescence and infrared imaging techniques has provided valuable insights into the condition of photovoltaic modules, particularly in detecting failures such as hot spots, snail trails and cell cracks. The presence of dark surrounding PV cells near junction boxes, as revealed by UV fluorescence, may indicate the accumulation of contaminants like dirt and dust.

- The use of EL imaging has proven to be a valuable tool for the detection of specific defects, such as broken cells, which can significantly affect the output power of the PV panel.

On the whole, this comprehensive approach underscores the importance of utilizing a variety of inspection methods to accurately diagnose and resolve failures in order to optimize the performance and longevity of the photovoltaic modules.

### Acknowledgements

This work was supported by The World Academy of Sciences-UNESCO under research grant number (No. 22-113RG/PHYS/AF/AC\_I) FR 324032455. The completion of certain parts of the article was achievable thanks to the ANRT funding and the co-funding between Heliocity and CSTB for the project “Methodology development to guarantee building photovoltaic systems’ performance including failure modeling” and by the French National Research Agency, through the Investments for Future Program (ref. ANR 18 EURE 0016 Solar Academy). Also, the authors wish to express their sincere gratitude to Mrs. Wilhelmina Logerais, a native English speaker, for her valuable contribution to proofreading this article. Her expertise and assistance in refining the language and clarity of the manuscript are greatly appreciated.

### Funding

This work was funded by The World Academy of Sciences-UNESCO (TWAS-UNESCO) under research grant number (No. 22-113RG/PHYS/AF/AC\_I) FR 324032455.

### Conflicts of interest

All the authors certify that they have no affiliations with or involvement in any organization or entity with any financial interest or non-financial interest in the subject matter or materials discussed in this manuscript.

### Data availability statement

Research data are not shared.

### Author contribution statement

All the authors were involved in the preparation of the manuscript. All the authors have read and approved the final manuscript.

### References

1. G. Masson, I. Kaizuka, E. Bosch, P. Macé, G. Masson, A. Van Rechem, C. Plaza, M. de l’Epine, A. Jäger-Waldau, J. Lindahl, A.O. Westerberg, Trends in photovoltaic applications, IEA PVPS, IEA-PVPS T1-43:2023, 2023
2. Renewable energy statistics 2020, 02-Jul-2020. <https://www.irena.org/publications/2020/Jul/Renewable-energy-statistics-2020>. [Accessed: 14-Mar-2024]

3. N. Bansal, S.P. Jaiswal, G. Singh, Comparative investigation of performance evaluation, degradation causes, impact and corrective measures for ground mount and rooftop solar PV plants – a review, *Sustain. Energy Technol. Assess.* **47**, 101526 (2021)
4. V. Sharma, O.S. Sastry, A. Kumar, B. Bora, S.S. Chandel, Degradation analysis of a-Si, (HIT) hetero-junction intrinsic thin layer silicon and m-C-Si solar photovoltaic technologies under outdoor conditions, *Energy* **72**, 536 (2014)
5. M. Bolinger, W. Gorman, D. Millstein, D. Jordan, System-level performance and degradation of 21 GW DC of utility-scale PV plants in the United States, *J. Renew. Sustain. Energy* **12**, 043501 (2020)
6. D.C. Jordan, B. Marion, C. Deline, T. Barnes, M. Bolinger, PV field reliability status—analysis of 100 000 solar systems, *Prog. Photovolt. Res. Appl.* **28**, 739 (2020)
7. D.C. Jordan, K. Anderson, K. Perry, M. Muller, M. Deceglie, R. White, C. Deline, Photovoltaic fleet degradation insights, *Prog. Photovolt. Res. Appl.* **30**, 1166 (2022)
8. D. Jordan, S. Kurtz, K. VanSant, J. Newmiller, Compendium of photovoltaic degradation rates, *Prog. Photovolt. Res. Appl.* **24**, 978 (2016)
9. C. Deline, K. Anderson, D. Jordan, A. Walker, J. Desai, K. Perry, M. Muller, B. Marion, R. White, PV fleet performance data initiative: performance index-based analysis (No. NREL/TP-5K00-78720) National Renewable Energy Lab.(NREL), Golden, CO (United States), (2021)
10. M. Green, Improving efficiency of PV systems using statistical performance monitoring, IEA, Technical Report IEA-PVPS T13-19:2021, Jul. 2017
11. M. Aghaei, A. Fairbrother, A. Gok, S. Ahmad, S. Kazim, K. Lobato, G. Oreski, A. Reinders, J. Schmitz, M. Theelen, P. Yilmaz, J. Kettle, Review of degradation and failure phenomena in photovoltaic modules, *Renew. Sustain. Energy Rev.* **159**, 112160 (2022)
12. K.-A. Weiß, L.S. Bruckman, R.H. French, G. Oreski, T. Tanahashi, Service life estimation for photovoltaic modules, IEA PVPS T13, IEA-PVPS T13-16:2021, 2021
13. M. Catelani, L. Ciani, L. Cristaldi, M. Faifer, M. Lazzaroni, Electrical performances optimization of photovoltaic modules with FMECA approach, *Measurement* **46**, 3898 (2013)
14. I. Kaaya, M. Köhl, A.-P. Mehilli, M. Sidrach-de-Cardona, K. Weiss, Modeling outdoor service lifetime prediction of PV modules: effects of combined climatic stressors on PV module power degradation, *IEEE J. Photovolt.* **9**, 1105 (2019)
15. I. Kaaya, J. Ascencio-Vásquez, K.-A. Weiss, M. Topič, Assessment of uncertainties and variations in PV modules degradation rates and lifetime predictions using physical models, *Sol. Energy* **218**, 354 (2021)
16. M. Herz, G. Friesen, U. Jahn, M. Köntges, S. Lindig, D. Moser, Quantification of technical risks in PV power systems, IEA PVPS, IEA-PVPS T13-23:2021, Feb. 2022
17. C. Miquel, C. Stravrou, N. Lebert, J. Sarantou, Dysfonctionnement électriques des installations photovoltaïques: points de vigilance, AQC – HESPUL, PTVIGI 1801, Oct. 2018
18. L. Bun, Détection et localisation de défauts dans un système photovoltaïque, PhD Thesis, Université de Grenoble, 2011
19. A. Mathieu, G. Fraisse, M. Thebault, S. Thebault, S. Boddart, L. Gaillard, *Failure risk analysis of photovoltaic systems based on literature review* (Eurosun 2022, Kassel, Germany, 2022)
20. A. Ndiaye, C.M.F. Kébé, A. Charki, P.A. Ndiaye, V. Sambou, A. Kobi, Degradation evaluation of crystalline-silicon photovoltaic modules after a few operation years in a tropical environment, *Sol. Energy* **103**, 70 (2014)
21. N. Kahoul, M. Houabes, M. Sadok, Assessing the early degradation of photovoltaic modules performance in the Saharan region, *Energy Convers. Manage.* **82**, 320 (2014)
22. M.R. Maghami, H. Hizam, C. Gomes, M.A. Radzi, M.I. Rezadad, S. Hajighorbani, Power loss due to soiling on solar panel: a review, *Renew. Sustain. Energy Rev.* **59**, 1307 (2016)
23. P. Sánchez-Friera et al, Analysis of degradation mechanisms of crystalline silicon PV modules after 12 yr. of operation in Southern Europe, *Prog. Photovolt.: Res. App.* **9**, 658 (2011). <https://onlinelibrary.wiley.com/doi/abs/10.1002/pip.1083>
24. M. Islam, Md. M. Rahman, A.H.M.Z. Karim, A. Ronee, Effects of natural dust on the performance of PV panels in Bangladesh, *Int. J. Mod. Educ. Comput. Sci.* **10**, 26 (2012)
25. S.A. Sulaiman, H.H. Hussain, N.S.H.N. Leh, M.S.I. Razali, Effects of dust on the performance of PV panels, *Int. J. Mech. Mechatron. Eng.* **5**, 2021 (2011)
26. U. Jahn, B. Herteleer, C. Tjendrawira, I. Tsanakas, M. Richter, G. Dickeson, A. Astigarraga, T. Tanahashi, F. Valencia, M. Green, A. Anderson, B. Stridh, A.R. Lagunas, S. Navarra, Y. Sangpongsanont, Guidelines for operation and maintenance of photovoltaic power plants in different climates, IEA, Technical Report IEA-PVPS T13-07:2022, Oct. 2022
27. W. Hermann, G. Eder, B. Farnung, G. Friesen, M. Köntges, B. Kubicek, O. Kunz, H. Liu, D. Parlevliet, I. Tsanakas, J. Vedde, Qualification of photovoltaic (PV) power plants using mobile test equipment, IEA PVPS T13, IEA-PVPS T13-24: 2021, Apr. 2021
28. C. Miquel, C. Stravrou, N. Lebert, J. Sarantou, Méthodes de détection des dysfonctionnements électriques des installations photovoltaïques, AQC – HESPUL, ETUC2P 1901, Jun. 2019
29. M. Köntges, S. Kurtz, C. Packard, U. Jahn, K.A. Berger, K. Kato, T. Friesen, H. Liu, M. Van Iseghem, Review of failures of photovoltaic modules, IEA PVPS T13, IEA-PVPS T13-01:2014, 2014
30. S. Rapaport, M. Green, The use of advanced algorithms in PV failure monitoring, IEA, Technical Report IEA-PVPS T13-19:2021, Sep. 2021
31. D.H. Daher, L. Gaillard, M. Amara, C. Ménézo, Impact of tropical desert maritime climate on the performance of a PV grid-connected power plant, *Renew. Energy* **125**, 729 (2018)
32. D.H. Daher, L. Gaillard, C. Ménézo, Experimental assessment of long-term performance degradation for a PV power plant operating in a desert maritime climate, *Renew. Energy* **187**, 44 (2022)
33. Solmetric, Solmetric PV Analyzer PVA- 1000 S
34. D.H. Daher, M. Aghaei, D.A. Quansah, M.S. Adaramola, P. Parvin, C. Ménézo, Multi-pronged degradation analysis of a photovoltaic power plant after 9.5 yr. of operation under hot desert climatic conditions, *Prog. Photovolt. Res. Appl.* **31**, 888 (2023)
35. W.D. Soto, S.A. Klein, W.A. Beckman, Improvement and validation of a model for photovoltaic array performance, *Sol. Energy* **80**, 78 (2006)

36. B. Li, C.W. Hansen, X. Chen, D. Diallo, A. Migan-Dubois, C. Delpha, A. Jain, A robust I-V curve correction procedure for degraded photovoltaic modules, *Renew. Energy* **224**, 120108 (2024)
37. B. Li, A. Migan-Dubois, C. Delpha, D. Diallo, Evaluation and improvement of IEC 60891 correction methods for I-V curves of defective photovoltaic panels, *Sol. Energy* **216**, 225 (2021)
38. IEC, IEC 6089 1: Photovoltaic devices – Procedures for temperature and irradiance corrections to measured I-V characteristics, Oct-2021
39. B. Li, Repo Github IVcorrection, lbj 2011 / IVcorrection. <https://github.com/lbj2011/IVcorrection>. [Accessed: 06-Mar-2024]
40. IEC, IEC 61829: Photovoltaic (PV) array –On-site measurement of current-voltage characteristics, Oct-2016
41. M. Köntges, A. Morlier, G. Eder, E. Fleiß, B. Kubicek, J. Lin, Review: ultraviolet fluorescence as assessment tool for photovoltaic modules, *IEEE J. Photovolt.* **10**, 616 (2020)
42. V.E. Puranik, R. Kumar, R. Gupta, Progress in module level quantitative electroluminescence imaging of crystalline silicon PV module: a review, *Sol. Energy* **264**, 111994 (2023)
43. M. Millendorf, E. Obropta, N. Vadhavkar, *Infrared solar module dataset for anomaly detection* (2020)
44. P. Wang, F. En, P. Wang, Comparative analysis of image classification algorithms based on traditional machine learning and deep learning, *Pattern Recognit. Lett.* **141**, 61 (2020)
45. V. Garchar, S. Chudhary, Image classification using advanced CNN based on tensorflow, *Int. J. Sci. Res. Comput. Sci. Eng. Inf. Technol.* **5**, 1329 (2019)
46. A.M. Hafiz, S.A. Parah, R.U.A. Bhat, Attention mechanisms and deep learning for machine vision: a survey of the state of the art, 2021, arXiv:2106.07550. <https://arxiv.org/abs/2106.07550>
47. M. Shaha, M. Pawar, Transfer learning for image classification, in *2018 Second International Conference on Electronics, Communication and Aerospace Technology (ICECA, 2018)*, pp. 656–660
48. V. Sharma, S.S. Chandel, A novel study for determining early life degradation of multi-crystalline-silicon photovoltaic modules observed in western Himalayan Indian climatic conditions, *Sol. Energy* **134**, 32 (2016)
49. S. Lindig, J. Ascencio-Vásquez, J. Leloux, D. Moser, A. Reinders, Performance analysis and degradation of a large fleet of PV systems, *IEEE J. Photovolt.* **11**, 1312 (2021)

**Cite this article as:** Daha Hassan Daher, Alexandre Mathieu, Asma Abdallah, Dek Mouhoumed, Pierre-Olivier Logerais, Leon Gaillard, Christophe Ménézo, Photovoltaic failure diagnosis using imaging techniques and electrical characterization, *EPJ Photovoltaics* **15**, 25 (2024)